

Research Article

Research on Mesoscopic Response of Asphalt Pavement Structure under Vibration Load

Zhanyou Yan ^{1,2}, Enli Chen,² Zhen Wang,² and Chundi Si²

¹School of Civil Engineering, Shijiazhuang Tiedao University, Shijiazhuang 050043, Hebei, China

²Key Laboratory of Traffic Safety and Control in Hebei Province, Shijiazhuang Tiedao University, Shijiazhuang 050043, Hebei, China

Correspondence should be addressed to Zhanyou Yan; yanzhanyou@163.com

Received 31 December 2018; Accepted 17 January 2019; Published 14 February 2019

Academic Editor: Roberto Palma

Copyright © 2019 Zhanyou Yan et al. This is an open access article distributed under the Creative Commons Attribution License, which permits unrestricted use, distribution, and reproduction in any medium, provided the original work is properly cited.

The various damages of asphalt pavement are closely related to the mesomechanical gradual behavior of asphalt materials, and it is very important to study the mesoscopic response under vibration loading in order to reveal the failure mechanism of asphalt pavement. The semisinusoidal vertical load is applied to the subgrade-surface discrete element model in this paper, and we use the model to analyze the evolution behavior of microcrack generation and expansion processes, stress distribution and stress transfer, and displacement field in various structural layers of asphalt pavement. The results show that the number of cracks increases rapidly on both sides of the vibration load, the rut is generated due to repeated load on the wheel, the asphalt mixture has bulging phenomenon on both sides of the rut and formed macroscopic cracks at the ridge, the microcracks extend mainly along the weak joints of the edges of the coarse aggregate and the asphalt cement, the number of microcracks increases slowly at the initial stage of the vibration load, the microcracks increase sharply until macroscopic cracks appear with the vibration load increases, the direction of compressive stress extends parallel to the microcrack, and the direction of tensile stress extends perpendicular to the microcracks inside the asphalt pavement. The results show that the discrete element method can not only obtain the stress and displacement of each structural layer, but also reveal the microcrack gradual behavior between particle flows.

1. Introduction

Asphalt pavement is generally composed of an asphalt layer, a cement stabilized layer, and a road base layer; the asphalt layer is mainly composed of asphalt, coarse aggregate, fine aggregate, and mineral powder; the cement stabilizing layer is composed of coarse aggregate, fine aggregate, and cement; the roadbed is mainly composed of earth and stone [1]. Therefore, the overall pavement structure is a heterogeneous and non-continuous body, the stress-strain is discontinuous, and the deformation is very complicated in the pavement structure under the load of the vehicle; if continuous medium mechanics is used to analyze the internal structural stress of the pavement, the actual deformation and stress state cannot be truly reflected inside the pavement structure [2, 3]. At present, many scholars have proposed applying the micromechanical theory to solve macroscopic mechanical problems, and micromechanical research has gradually become an area of scientific focus [4].

Macroscopic mechanics often adopts the traditional continuum mechanics theory, which assumes that the structural layers inside the subgrade are the same homogeneous body, and the geometric and physical characteristics, such as aggregate shape, spatial position, aggregate texture, and aggregate gradation, are ignored; however, the internal geometry and physical properties are of great importance to the overall performance of the pavement structure layer [4–7]. The existing discrete element theory holds that each structural layer is composed of particles of different sizes and shapes; the particles are rigid bodies, and the deformation is caused by the overlapping of the particles; the particles are in contact with each other, and the force can only be transmitted by the contact of the particles; the bonding relationship can be set between the particles, and the force can be determined by Newton's second law; the action of particles is a dynamic process, and the application of external force will cause a certain range of particles to move and rotate, it takes a long

time to reach equilibrium between particles [8–12]. Some scholars and experts have made research and exploration at home and abroad; for example, Kim et al. [13, 14] took a series of deformation pictures of asphalt mixture in different time periods through CT scanning technology and established the finite element model by using mesomechanics and fracture mechanics theory to analyze the mechanism of macrocrack generation of specimens. Mahmoud et al. [3] followed the principle of constant mass ratio and specific surface area and treated less than 4.75 mm particles inside the mixture as asphalt cement material; the distribution of aggregates was obtained by CT scanning in the asphalt mixture. Eckwright et al. [15] established the AC-16 uniaxial compression model of asphalt mixture by FISH language and analyzed the regularity of particle flow stress-strain, contact force, particle displacement, contact pressure, and tensile force. At present, it can be understood from the above that most of the research on the mesomechanical behavior of asphalt pavement is concentrated on the test of small-scale asphalt layer test pieces and analyzes the mesomechanical constitutive relation and mechanical behavior of small-scale asphalt mixture specimens under static load [16–18]; however, it is still rare to analyze the mesoscopic response and microcrack grading behavior for large-scale specimens (pavement overall structure layer) and involving vibration load in the existing literature.

In this paper, according to the actual pavement structure hierarchy, and using the combination of the random placement algorithm and porosity treatment principle, the two-dimensional subgrade-pavement discrete element model is established by using the FISH language in the PFC2D software and the mesoscopic parameters of each structural layer are obtained by comparing the standard uniaxial compression stress-strain test of materials with the uniaxial compression test of the established model. Semi-sinusoidal vertical load is applied to simulate vehicle loading and unloading; reveal the relationship between the microcrack propagation process, mesoscopic failure, and the macroscopic dynamic response of each structural layer; and analyze the mesoscopic response gradation behavior of asphalt pavement under vibration loading; these research results provide a reference for the mechanism of pavement damage.

2. Materials and Methods

According to the literature research [19–23], a typical pavement structure model is applied and the model is divided into six layers, including upper layer, lower layer, upper base layer, lower base layer, bottom base layer, and subgrade. The roadbed mainly bears and disperses the vehicle load, the vehicle load is relatively small under the roadbed, and the depth of roadbed is 80 cm in the specification. Since the model uses large-scale test pieces, the depth of the roadbed is determined to be 100 cm in order to reduce the calculation amount of the model, the material of the pavement structure layer is composed of different particle size streams, and the particles are in contact with the particles between the layers. The pavement structure parameters are shown in Table 1.

TABLE 1: Pavement structural parameters.

Material name	Depth (cm)	Structural layer location
SMA-13	4	Upper layer
AC-20	11	Lower layer
5% cement stabilized gravel	16	Upper base layer
5% cement stabilized gravel	16	Lower base layer
4% cement stabilized grit	18	Bottom base layer
Earth and stone	100	Subgrade

A variety of common contact models are provided in the PFC2D software. The linear parallel bond model can reflect the internal mechanical relationship between the binding material and the coarse aggregate, and parallel bonding model calculation is relatively simple [24, 25]. The particle flow model and the mechanical relationship are shown in Figure 1.

$$\left\{ \begin{array}{l} \bar{F}_j = \bar{F}_j^n + \bar{F}_j^s \\ \bar{M}_j = \bar{M}_j^n + \bar{M}_j^s \end{array} \right\}. \quad (1)$$

Figures 1(a) and 1(b) illustrate contact particles; $x_i^{[A]}$, $x_i^{[B]}$, and $x_i^{[C]}$ illustrate the centers of particles A and B and the bonding point; \bar{F}_j is the representative of parallel bond model force; \bar{M}_j represents the parallel bond model moment. The internal forces and moments are all zero when the model is calculated to reach equilibrium; \bar{F}_j^n is decomposed into normal force, \bar{F}_j^s is decomposed into tangential force, \bar{M}_j^n is decomposed into normal moment, and \bar{M}_j^s is decomposed into tangential moment [26, 27].

We have corresponding force and bending moment increment when the particles are displaced:

$$\begin{aligned} \Delta \bar{F}_j^n &= (-\bar{k}^n A \Delta u_n) n_i, \\ \Delta \bar{F}_j^s &= -\bar{k}^s A \Delta u_s, \\ \Delta \bar{M}_j^n &= -\bar{k}^n I \Delta \theta_n, \\ \Delta \bar{M}_j^s &= -\bar{k}^s I \Delta \theta_s, \end{aligned} \quad (2)$$

$$\bar{k}^n = \frac{\bar{k}_n^A \bar{k}_n^B}{\bar{k}_n^A + \bar{k}_n^B},$$

$$\bar{k}^s = \frac{\bar{k}_s^A \bar{k}_s^B}{\bar{k}_s^A + \bar{k}_s^B}.$$

In these equations, $A = \pi R^2$; I represents moment of inertia; Δu_n and Δu_s represent the particle's normal and tangential displacements; $\Delta \theta_n$ and $\Delta \theta_s$ represent the particle's normal and tangent relative rotation angles; \bar{k}^n represents the normal contact stiffness; \bar{k}^s represents the tangential contact stiffness; \bar{k}_n^A represents the normal contact stiffness of particle A; \bar{k}_s^A represents the tangential contact stiffness of particle A; \bar{k}_n^B represents the normal contact stiffness of particle B; \bar{k}_s^B represents the tangential contact stiffness of particle B; g_s represents the parallel key distance;

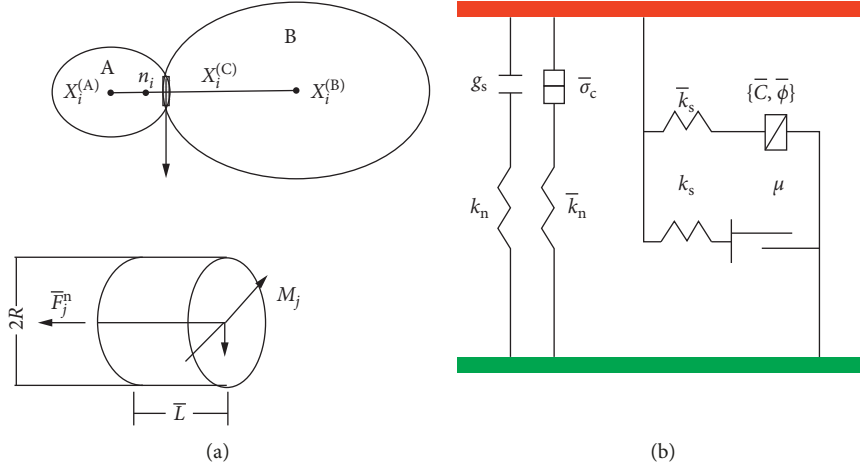


FIGURE 1: Linear parallel bond model. (a) Mechanical relationship between particles. (b) Mechanical relationship of linear parallel bond model.

$\bar{\sigma}_c$ represents the tensile stress between particles; μ represents the friction coefficient; k_s represents the tangential contact stiffness; \bar{c} represents cohesion; and $\bar{\phi}$ represents the internal friction angle [28].

Force and bending moment are updated according to the following formula where t represents time:

$$\begin{aligned}\bar{F}_j^n(t) &= \left| \bar{F}_j^n(t - \Delta t) \right| n + \Delta \bar{F}_j^n, \\ \bar{F}_j^s(t) &= \bar{F}_j^s(t - \Delta t) + \Delta \bar{F}_j^s, \\ \bar{M}_j^n(t) &= \left| \bar{M}_j^n(t - \Delta t) \right| n + \Delta \bar{M}_j^n, \\ \bar{M}_j^s(t) &= \bar{M}_j^s(t - \Delta t) + \Delta \bar{M}_j^s.\end{aligned}\quad (3)$$

So, we can obtain normal stress and tangential stress:

$$\begin{aligned}\sigma &= \frac{-\bar{F}_j^n}{A} + \frac{\bar{M}_j^s}{I} R, \\ \tau &= \frac{-\bar{F}_j^s}{A}.\end{aligned}\quad (4)$$

In the particle flow calculation process, the contact force and the unbalanced force are constantly balanced in the particle flow motion; microcracks are generated between particles when the tensile and shear resistance exceeds the bond strength in the model [29].

According to the theory of asphalt cement, the coarse aggregate (particle size greater than 2.36 mm) plays a skeleton role and bears most of the internal stress in the asphalt mixture, and the fine aggregate (particle size less than 2.36 mm) plays the role of filling skeleton space and binding between the coarse aggregates. In order to simplify the model and simplify the calculation data, we consider fine aggregate, water, and asphalt as binding materials, so the discrete element model only contains coarse aggregate and binding material particles [30–33].

Six spaces are generated and separated by walls using the PFC2D software, according to the actual structural material grading, the distribution area of the coarse aggregate is calculated and placed it in the wall step by step. The specific model is shown in Figure 2.

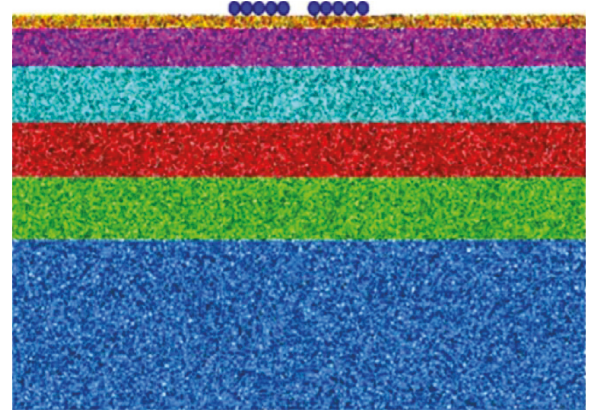


FIGURE 2: Discrete element model of subgrade and pavement structure.

3. Vibration Load Realization

The two-wheel set BZZ-100 is used as the standard load in the pavement design specification, the tire marks are actually elliptical; however, for the convenience of calculation, more circular tire marks are used in the model calculation, the tire load is regarded as the equivalent circular uniform load, and the internal pressure of the tire is used instead of the contact pressure at the bottom of the wheel. The specific values are shown in Table 2.

To simulate wheel load with CLUMP unit on the surface layer above the model, five PEBBLE units are used to represent one wheel, five PEBBLE units are tightly connected (21.3 cm in diameter), and the distance is 10.65 cm between the two CLUMP units (the upper layer of Figure 2). In order to accelerate the failure behavior of various structural layers, a semisinusoidal vertical load is applied to the CLUMP unit with a peak value of 100 kN and a cycle time of 0.06 s, and the model repeatedly applies periodic loads, eventually producing macroscopic cracks, the vibration load is performed by writing a subroutine in the FISH language within the PFC. The vibration load amplitude curve is shown in Figure 3.

TABLE 2: Design parameters of standard axle load.

Load name	Standard axle load, P (kN)	Ground tire pressure, P (MPa)	Equivalent circle diameter of single wheel pressure transmitting surface (cm)	Tire center distance (cm)
BZZ-100	100	0.7	21.3	1.5 d

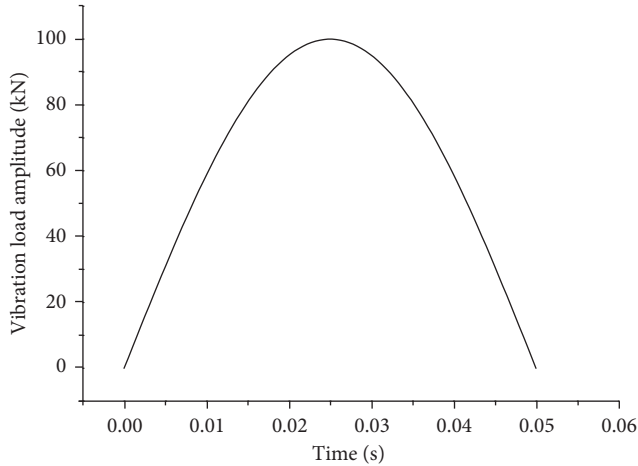


FIGURE 3: Amplitude curve of vibration load.

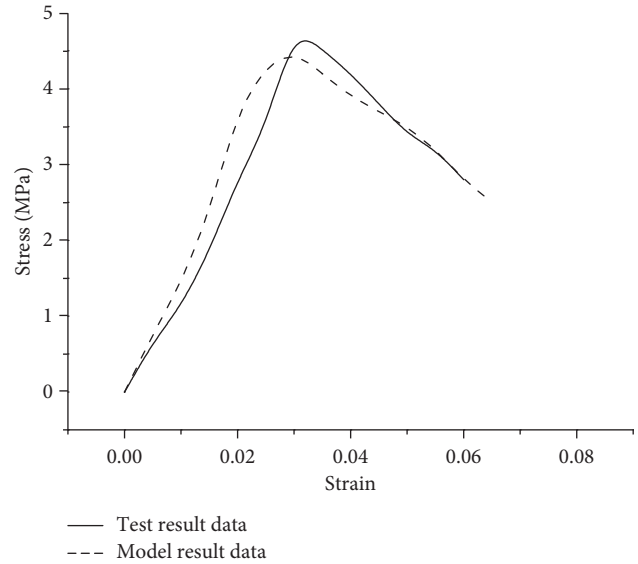


FIGURE 4: Stress-strain data of SMA-13 asphalt mixture.

4. Particle Flow Mesoscopic Parameters

In the literature, most experts and scholars believe that the macroscopic mechanical parameters cannot be directly applied to the discrete element model [34–36]; however, the macroscopic mechanical characteristics are closely related to the microscopic mechanics of discrete element models. At present, the stress-strain (load-displacement) curve is generally used to illustrate the relationship between macroscopic and mesoscopic mechanics, by comparing the results of compressive strength test in the laboratory with those of the discrete element model. The discrete element model mesoscopic parameters can be obtained by iterative calculation [37, 38]. Figure 4 shows the comparison between the uniaxial compression test data of the SMA-13 asphalt mixture and the model data; the model geometry is 80 mm × 40 mm. Figure 5 shows the SMA-13 asphalt mixture model and the entire process of destruction. Figure 6 shows the failure process of the uniaxial compression specimen of asphalt mixture under indoor standard conditions; the red line is the main crack extension line.

It is necessary to know the mesoscopic parameters (κ^* , $\bar{\sigma}_c$, \bar{c} , E) when we calculate the mesomechanical behavior of the discrete element model [39], it can be seen from Figure 4 that the uniaxial compression stress-strain curve is basically consistent with the experimental curve, and the stress peak error is less than 5.2%. Therefore, we can get the SEM-13 asphalt mixture discrete element mesoscopic parameters; the mesoscopic parameters of the remaining pavement materials are the same as those of the SMA-13 asphalt mixture. The microscopic parameters of the linear parallel bond model are shown in Table 3.

5. Results and Description

5.1. Microcrack Gradual Behavior. Applying a half-wave sinusoidal vertical load to the surface of the model, and gradually generating microcracks inside the pavement, microcrack density continues to increase with the load continues; finally, the microcracks penetrate each other to form macrocrack. Figures 7–10 show the whole process of microcrack generation in the model under vibration load.

It can be seen from Figure 7 that there is no obvious microcrack in the pavement structure from the upper part to the lower part when the vibration load reaches 1 s; this stage is represented by the compaction process of the particle flow in each structural layer, and the material properties exhibit elasticity, the density of the upper layer and the lower layer increases significantly, and the contact force of the particle flow increased significantly.

It can be seen from Figure 8 that microcracks appear in the upper layer and the lower layer when the vibration load reaches 2 s, microcracks are concentrated at both ends of the wheel load; at this time, the tensile stress is obviously increased at the bottom layer of the lower layer, and the microcracks appear as bond break between the particle streams, and the surface is slightly sunken on the upper layer.

It can be seen from Figure 9 that the number of microcracks increases significantly in the pavement when the vibration load reaches 4 s (blue indicates crack), a large number of microcracks are concentrated on both ends of the wheel load, and the microcrack develops vertically

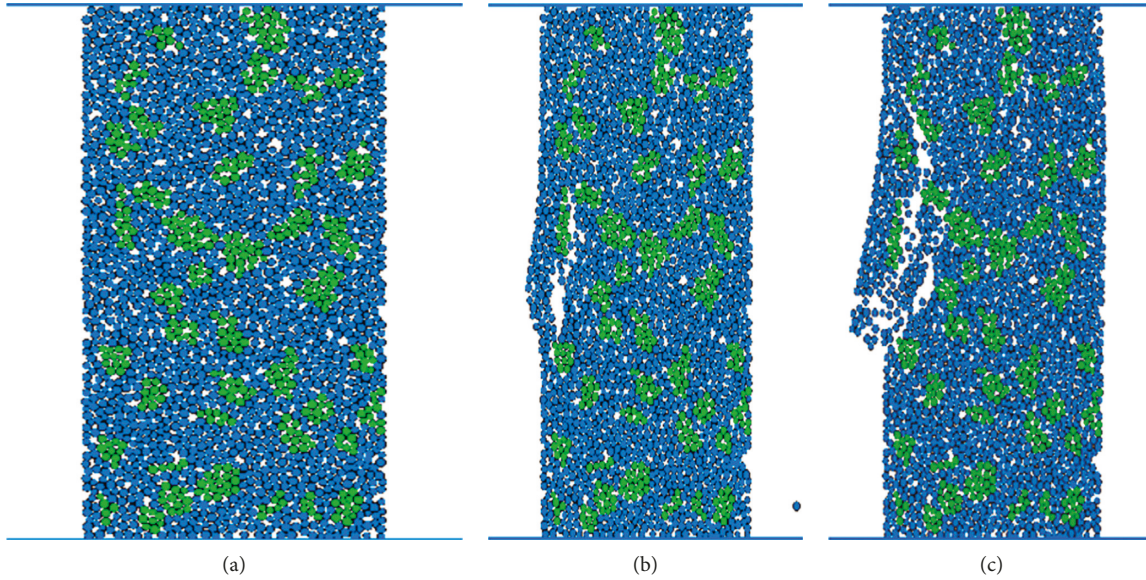


FIGURE 5: Single-axial compression failure model of SMA-13 asphalt mixture: (a) initial load model; (b) medium load model; (c) final load model.

downward and toward the sides. There is a slight rut in the upper layer, microcracks appear in the lower layer, and the bond key is basically destroyed at the bottom tension zone. Microcrack concentration occurs at the bottom of the upper base layer, and the microcrack width is larger than the bottom of the lower layer.

It can be seen from Figure 10 that there are more and more microcracks in the pavement structure when the vibration load reaches 12 s, and the microcracks density is getting larger and larger. The depth of the microcrack gradually extends to the subgrade, and the overall width of the microcrack and the surface subsidence of the pavement continues to increase. The functional diseases have occurred in the overall structure of the pavement when the vibration load reaches the end, and the microcracks of each structural layer are merged and penetrated to form macrocracks in addition to the subgrade. The macrocracks are dominated by the vertical direction. The width of the microcracks is increased by more than 2 times at the bottom of the lower layer, and these microcracks are the initial cause of the pavement structure damage.

By studying the whole process of microcrack propagation, it can be known that most of the microcracks expand along the shear stress direction under the double-wheel load, the number of microcracks is the highest at both ends of the load, the shape of microcracks is symmetrically distributed overall, and the microcrack density in the middle strong stress region of the load is much larger than the microcrack density at both ends of the load.

Figure 11 shows partial enlargement of the calculation time 4 s. It can be seen from Figure 11 that the wheel load portion has obvious rutting (middle part of the figure) with the calculation time increases, and the rut depth is about 0.043 mm. There is an asphalt mixture bulging on the outside of the wheel, and the phenomenon of bulging is more obvious on both sides with the load increases. There are two obvious

macrocracks on both sides of the rut, the microcrack on the left side maintains 40° curve extending from the horizontal direction among them and penetrates the upper base layer and gradually returns to the lower layer; the microcrack on the right side also maintains a 40° curve extending from the horizontal direction and passes through the surface of the lower layer; the model produces microcracks in different directions during the macrocrack propagation process.

Figures 12 and 13 are enlarged views of the internal macrocracks of the upper layer and the lower layer. It can be seen from the figure that macrocracks will be generated inside the upper layers and lower layers with the load increases, the initial macrocrack expands along the rough aggregate surface and the weakest edge of the asphalt cement, and the coarse aggregate particles are almost not broken and the macrocrack gradually penetrates the asphalt cement, eventually leading to macrocracks. The second crack will be generated at the crack extension stress concentration with the load continuing to increase, and the remaining cracks will develop like this; eventually, the microcracks are distributed throughout the entire area, and microcracks are merged in different directions.

From the trend of microcrack generation and expansion, it is known that the combination is the main weak part of asphalt mixture between coarse aggregate and asphalt cement, which is easy to produce early microcracks; microcracks eventually become macroscopic cracks under continuous vehicle loading. Functional conditions have already appeared in the pavement structure in this state, and we should protect it.

5.2. Microcracks Number Gradual Behavior. Figure 14 shows the relationship between the number of microcracks and the load time. It can be seen from the figure that the number of microcracks is continuously increasing in the model, the



FIGURE 6: Single-axial compression test of SMA-13 type asphalt mixture: (a) initial compression stage; (b) medium compression stage; (c) final compression phase; (d) terminal compression crack.

growth rate of microcracks is relatively large in the 0–8 s stage, which shows a linear relationship, and the growth rate of microcracks is relatively small in the 8–12 s stage, which presents a nonlinear relationship.

It can be seen from the above figure that there is almost no microcrack inside the 0–1 s phase discrete element model, stress is continuously transmitted between the particles, and

the stress continues to accumulate and self-adjust, eventually reaching dynamic equilibrium. A small number of microcracks appear inside the 1 s–2 s stage discrete element model, and the number of microcracks is very small, most of the macroscopic physical and mechanical performance indicators are not damaged in this state. The number of microcracks increases rapidly inside the 2 s–8 s stage, and the length of

TABLE 3: Microscopic parameters of linear parallel bond model in the asphalt mixture.

Structural layer location		Particle density ($\text{kg}\cdot\text{m}^{-3}$)	Stiffness ratio between tensile and shear, κ^*	Tensile strength, $\bar{\sigma}_c$ (Pa)	Cohesion, \bar{c} (Pa)	Particle elastic modulus, E (Pa)	Particle radius (mm)
Upper layer	Coarse aggregate	2500	1	$4.2e9$	$2.3e10$	$6.3e9$	0.5–0.75
	Binding material particles	2100	1	$4.4e6$	$5.2e6$	$5.9e8$	0.5–0.75
Lower layer	Coarse aggregate	2500	0.8	$6.1e9$	$1.85e10$	$6.5e9$	0.75–1
	Binding material particles	2100	0.8	$5.4e6$	$6.2e6$	$7.8e8$	0.75–1
Upper base layer		2400	1	$8.3e6$	$9.7e6$	$4.3e8$	0.75–1
Lower base layer		2400	1	$6.9e6$	$8.1e6$	$4.4e8$	0.75–1
Bottom base layer		2200	1	$6.4e6$	$8.43e6$	$3.2e8$	0.75–1
Subgrade		1900	1	$1.5e6$	$5.4e6$	$6.4e8$	0.5–1

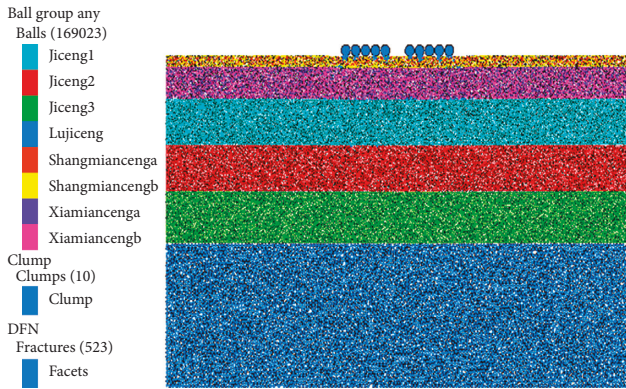


FIGURE 7: Microcrack shape in 1 second.

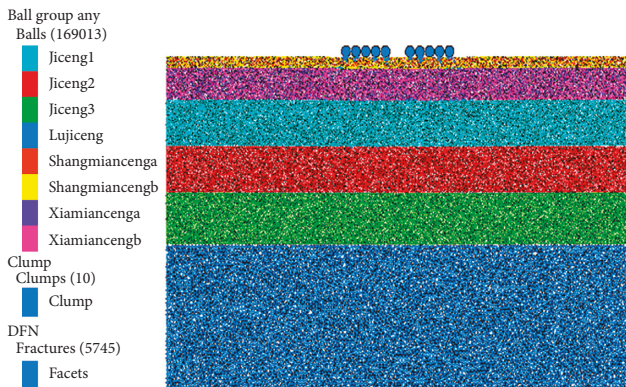


FIGURE 8: Microcrack shape in 2 seconds.

microcracks continued to increase. The number of microcracks is linear with the load time. The dynamic balance of the model is broken at this stage. Microcracks do not appear randomly, but spread rapidly downwards and outwards on both sides of the tire. Most of the microcracks cross each other and merge in this state, and the surface layer shows macroscopic cracks. The ability to resist external loads is much reduced in the model, and the rutting is gradually increasing. The number of microcracks is in a stationary phase inside 8 s–10 s stage, and the number of microcracks does not increase significantly. The number of microcracks has a certain increasing trend during the 10 s–12 s stage, but the rate of growth is small.

Due to external wheel vibration load, increasing microcracks have seriously changed the ability to withstand external loads; if the model is subjected to wheel loads for a long time, the particle flow cannot be completely restored to its original state, and the asphalt pavement is already in an initial destruction state.

5.3. Structural Layer Stress Response. Since the discrete element model is a point contact between particles, the particle flow will continue to shift and rotate under the continuous vibration load of the wheel, stress is transmitted between the particles, and the change of stress reflects the macroscopic structural mechanical properties in the discrete element model. The stress is closely related to the microcracks generation, microcracks expansion, and microcracks penetration in particles.

Figure 15 shows the overall force chain diagram for the asphalt pavement model. The blue color represents the compressive stress between the particles in the figure, and the red color represents the tensile stress between the particles in the figure; the color thickness represents the magnitude of the stress. It can be seen that most of the pavement structure exhibits compressive stress from Figure 15, and the compressive stress is arranged in a layer pattern (blue layering) in the overall model, and the pressure layer style is “U” type. The direction of the compressive stress is vertically downward in the middle, and the direction of the compressive stress is outwardly distributed on both sides. The red color part (tensile stress) exists in the form of dots, and the tensile stress of individual red parts is relatively dense, the red part accounts for about 43% in the upper layer load area, and the interaction force between particles shows both tensile stress and compressive stress in the upper layer. The red color is relatively heavy and forms a “U” shape at the bottom of the lower layer, and the red part accounts for about 60–70%. The tensile stress is distributed outward and downward at 40 degrees from the horizontal direction; this is closely related to the number of microcracks generated at the bottom of the lower layer. The tensile stresses are distributed in a point in the upper base layer and the lower base layer, and the tensile stress accumulation is not obvious. There is tensile stress concentration on the contact surface between the bottom base layer and the subgrade, which is closely related to the density of the microcracks on the contact surface. The tensile stress is

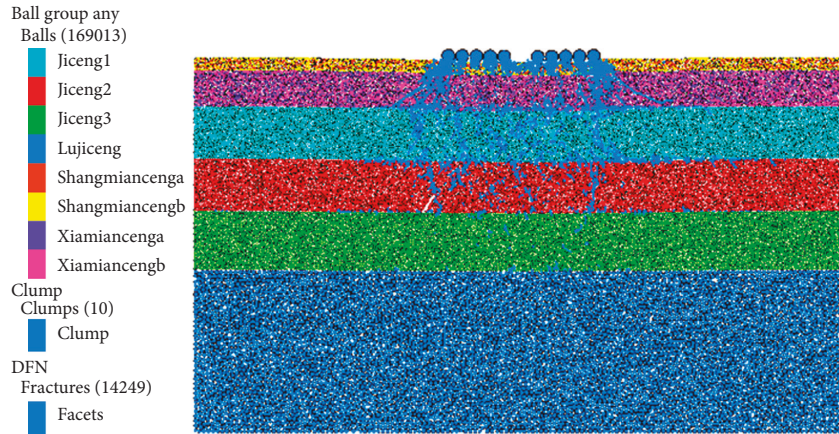


FIGURE 9: Microcrack shape in 4 seconds.

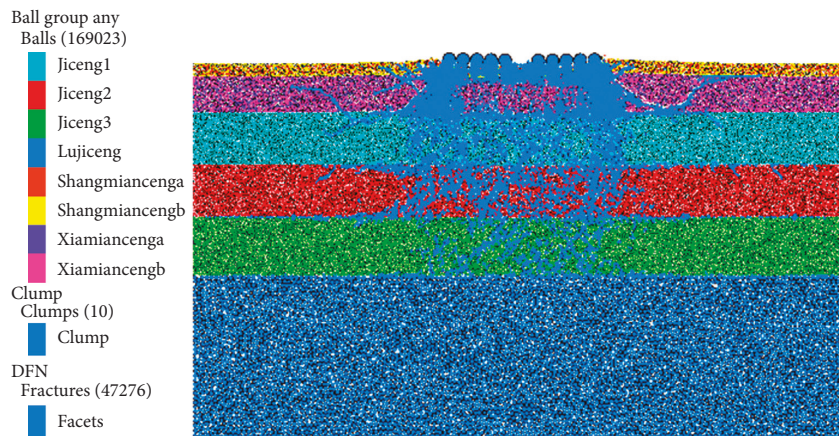


FIGURE 10: Microcrack shape in 12 seconds.

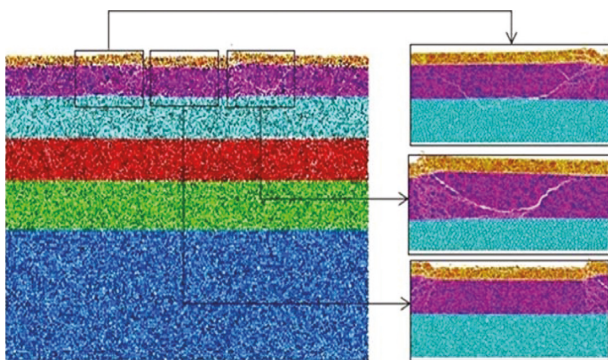


FIGURE 11: Macrocrack shape in 4 seconds.

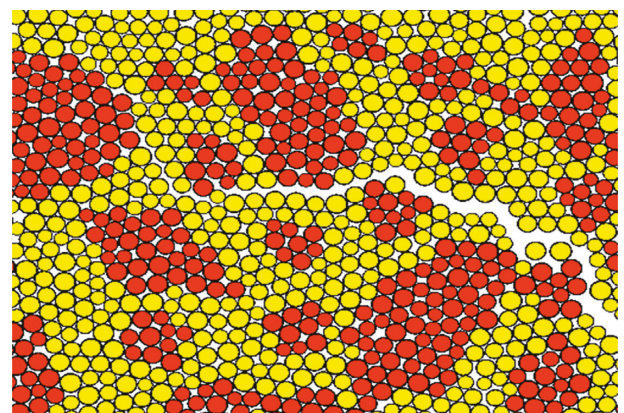


FIGURE 12: Local macrocrack extension of the upper surface layer.

a uniformly dispersed arrangement inside the subgrade, and the tensile stress concentration is rare, and the particles mainly show compressive stress.

Figure 16 shows the force chain diagram at the local crack in the upper layer. It can be seen from Figure 16 that the force chain is completely broken on both sides of the crack, and there is no relationship between the particles. The direction of the compressive stress extends parallel to the crack at the upper part of the crack, the starting load section (upper left corner) shows the tensile stress, and the tensile

stress extends to the lower right; the rest of the area exhibits compressive stress and compressive stress concentration at some locations (blue line concentration). The particles are mainly subjected to compressive stress under the crack, and the direction of the compressive stress extends parallel to the crack, the tensile stress is dispersed and produces tensile stress concentration phenomenon in some places of the model (red colour concentration point).

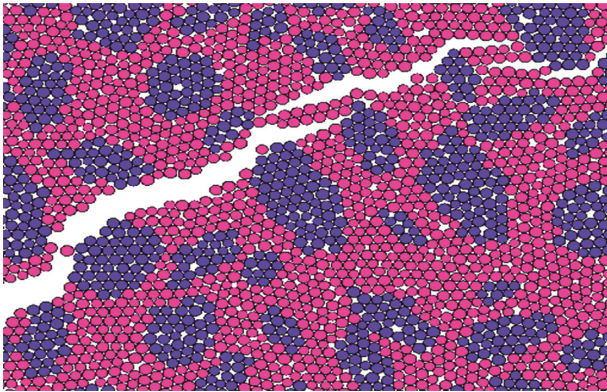


FIGURE 13: Local macrocrack extension of the lower surface layer.

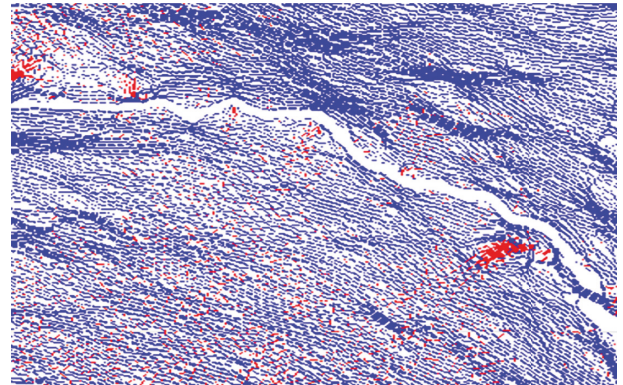


FIGURE 16: Force chain diagram near the crack in the upper layer.

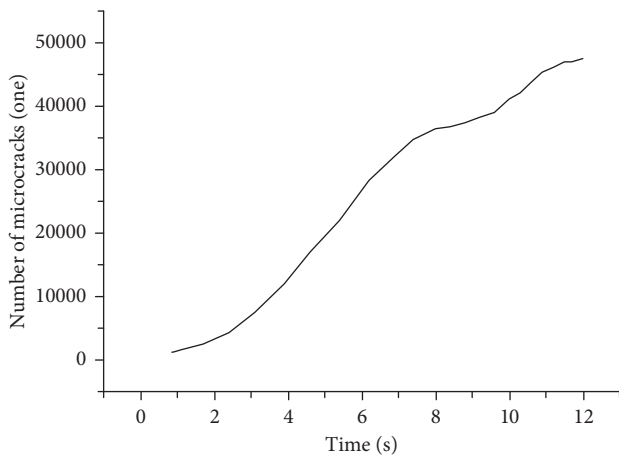
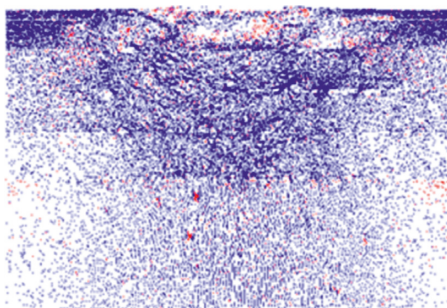


FIGURE 14: Relation curve of microcrack number and load time.



Contact force chain
 Contacts (432914)
 ■ Compression
 ■ Tension

FIGURE 15: Internal force chain diagram of the whole model.

Figure 17 shows the force chain diagram at the local crack in the lower layer. It can be seen from Figure 17 that the force chain is almost completely broken on both sides of the crack, and only a small part of the crack is connected together (2 positions). The compressive stress and the tensile stress exist simultaneously between the particles at the upper part of the crack, and tensile stress concentration occurs at the upper right layer near the upper layer (1 positions); the

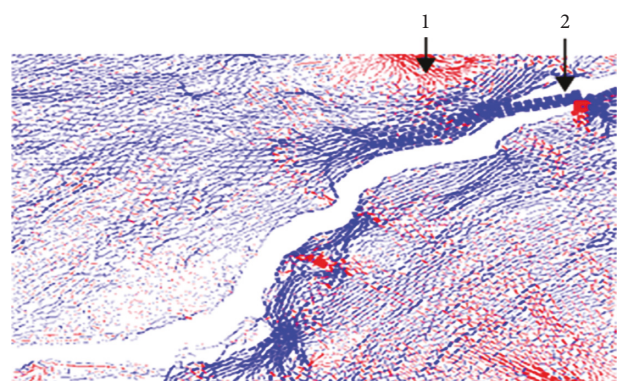


FIGURE 17: Force chain diagram of crack location in the lower layer.

direction of the compressive stress is collected to the upper right at the lower part of 1 position, and finally concentrated at the crack junction (2 positions), the tensile stress concentration (red position) appears in the lower right corner of the joint. The direction of the tensile stress is concentrated to the lower right corner under the crack, and the direction of the compressive stress is parallel to the direction of the crack, and the direction of compressive stress and direction tensile stress are perpendicular to each other.

5.4. Structural Layer Displacement Response. The particle flow will continue to shift and rotate under the continuous vibration load of the wheel, and the appearance of the model shows that the particles have a tendency to move around.

Figure 18 shows the overall displacement nephogram of the discrete element model. It can be seen from Figure 18 that the overall displacement nephogram shape is “U” type under vibration load, the displacement gradually decreases with the depth of the structural layer increases, the upper layer produces the largest displacement among them, and the displacement of the lower layer is smaller than the upper layer and the subgrade has almost no displacement. The surface of the upper layer continues to produce approximately 5.5 mm ruts, and particle bulging occurs on both sides of the rut; these phenomena are closely related to the formation of macroscopic cracks and force accumulation on both sides of the rut.

Figure 19 shows the displacement of the horizontal displacement of the asphalt pavement. The red color indicates

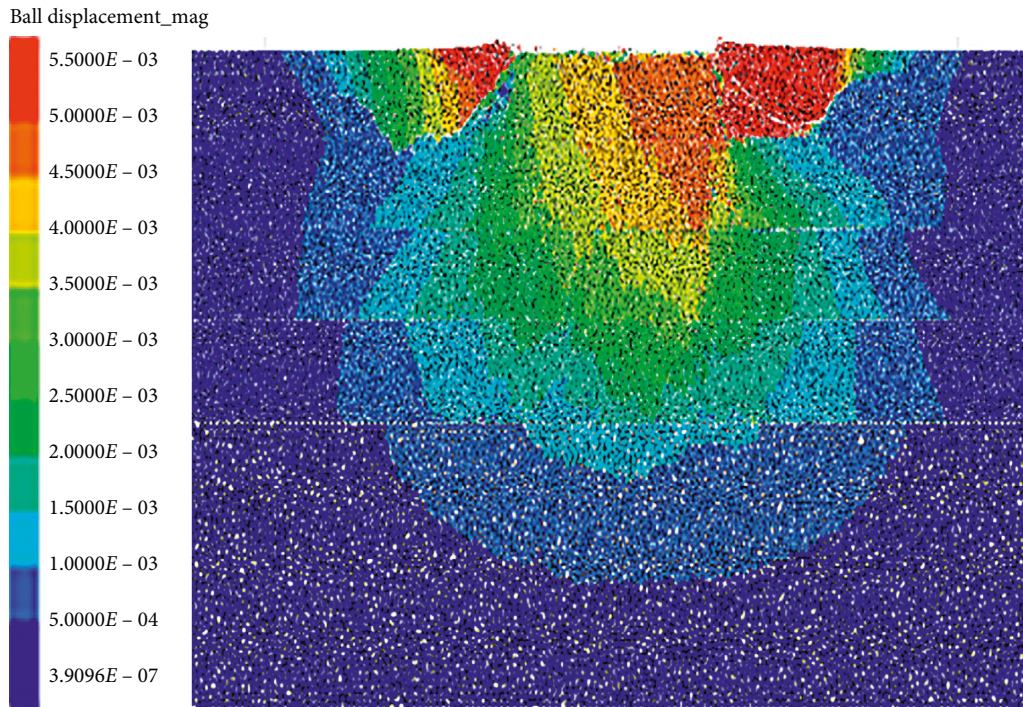


FIGURE 18: Overall displacement nephogram of discrete element model.

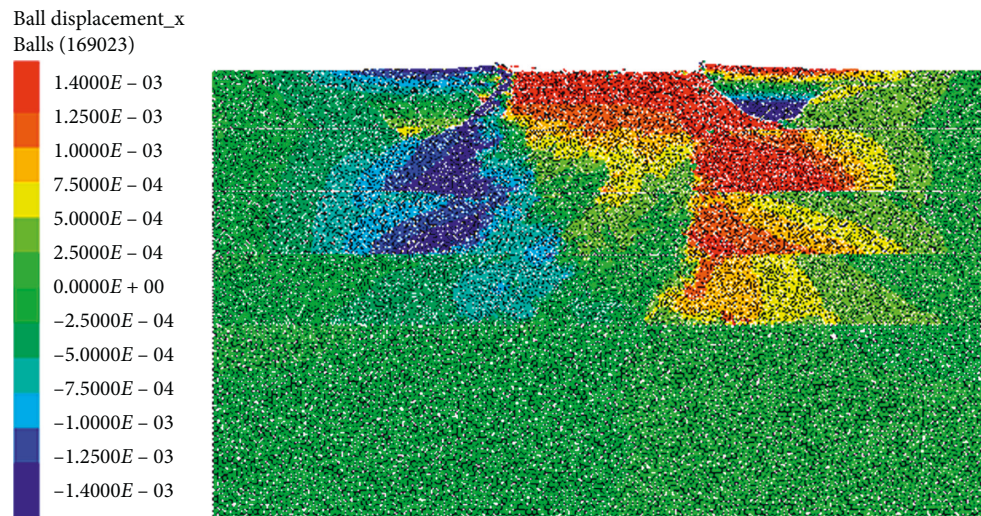


FIGURE 19: Horizontal displacement nephogram of discrete element model.

a positive direction displacement (positive in the right direction), and the blue color indicates a negative direction displacement (negative in the left direction). It can be seen from Figure 18 that the structural layers of the pavement have a certain horizontal displacement under vibration load; there is a clear separation between the layers of the pavement structure. The area of the layer contact surface is getting smaller and smaller with the depth of the structural layer increases, and the horizontal displacement is almost symmetrically arranged. The displacement is the largest (red color area) in the horizontal direction of the middle compression zone, and the displacement gradually decreases with the structural depth increases, The horizontal displacement of the

particles moves oppositely on the right side of the rutting area (the lower part is red and the upper part is blue), and the horizontal displacement of the particles moves in the same direction on the left side of the rut area (blue color). The horizontal displacement values are almost the same at the upper base layer and the lower base layer, and the particles move in opposite directions (red color and blue color). The horizontal displacement is the largest at the contact layer position, which is consistent with the maximum number of cracks and the maximum tensile stress at the contact layer, and the subgrade has almost no horizontal displacement.

Figure 20 shows the vertical displacement nephogram of the discrete element model. The red color indicates that the

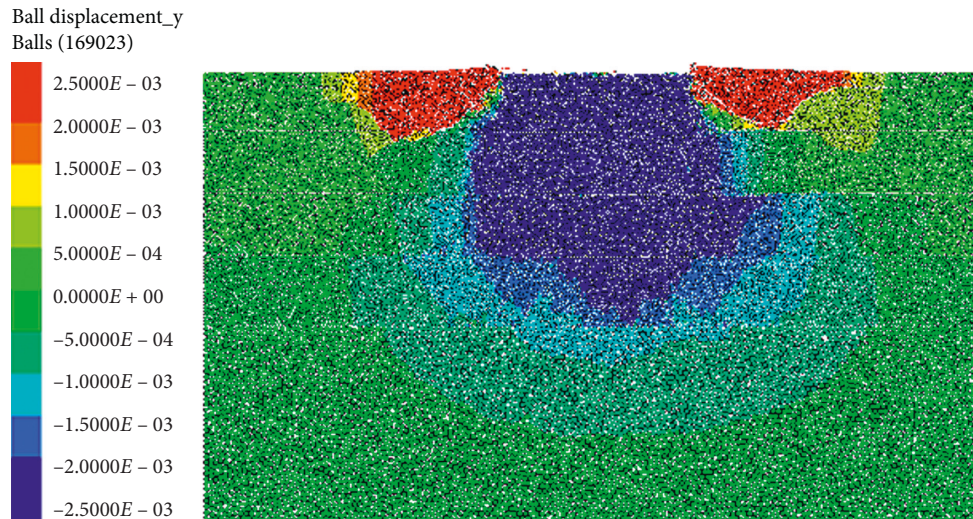


FIGURE 20: Vertical displacement nephogram of discrete element model.

displacement direction is upward. The red color indicates an upward displacement. The blue color indicates a downward displacement. It can be seen from Figure 20 that the particle flow has an upward movement tendency on both sides of the rutting area under vibration load. The red color area mainly occurs in the upper layer and the lower layer, and red color area symmetrically arranged. There is a clear dividing line between the red color and the green color, and the dividing line is a macrocrack. Most of the particle flow has a downward trend at the bottom of the rutting area, the displacement of the particle flow gradually decreases with road depth increases, and the particle flow also has a tendency to move to both sides under the action of wheel load.

6. Conclusion

By comparing the indoor standard uniaxial compression test with the discrete element model, we can obtain the mesoscopic parameters of each structural layer and establish a discrete element model of the pavement structure and the mesoscopic response gradual behavior of the pavement under the given vibration load. The results show that the initial crack growth is slow in the particle flow under the action of vibration load and the crack growth is faster in the later stage, which eventually leads to rutting on the surface of the model. Most of the cracks extend along the shearing direction in the particle streams, and there are many cracks at the bottom of the wheel, and the cracks are almost symmetrically arranged. Most of the fine cracks extend along the edge of the coarse aggregate and the weakness of the asphalt cement in the particles under the action of vibration load; eventually, microcracks merge into macroscopic cracks in different directions. The force chain pattern is “U” type in the particles under the action of vibration load, which has both compressive and tensile stresses. The upper layer and the lower layer mainly exhibit tensile stress, and the other regions exhibit compressive stress; the particles are completely separated on both sides of the crack. The upper layer particles have the largest displacement under the action of

vibration load, the displacement gradually decreases with road depth increases, and the subgrade has almost no displacement. The horizontal displacement layer has obvious boundary and has a tendency toward both sides, and the horizontal displacement is symmetrically arranged; the particle flow has a bulging phenomenon on both sides of the rut area. The discrete element model can not only obtain the stress and displacement under the action of vibration load, but also obtain the variation trend between the particles; the discrete element model can express both macroscopic mechanical behavior and mechanical mesoscopic behavior.

Data Availability

The data used to support the findings of this study are available from the corresponding author upon request.

Conflicts of Interest

The authors declare no conflicts of interest.

Authors' Contributions

Z.Y. and E.C. conceived the algorithm and designed experiments; Z.W. implemented the experiments and processed test data; and C.S. analyzed the results. All authors read and revised the manuscript.

Acknowledgments

This research was funded by the National Natural Science Foundation of China (grant 11172183) and Central Guided Local Science and Technology Development Project of China (18242219G).

References

- [1] Y. Liu and Z. You, “Visualization and simulation of asphalt concrete with randomly generated three-dimensional

- models,” *Journal of Computing in Civil Engineering*, vol. 23, no. 6, pp. 340–347, 2009.
- [2] Y. Liu and Z. You, “Accelerated discrete-element modeling of asphalt-based materials with the frequency-temperature superposition principle,” *Journal of Engineering Mechanics*, vol. 137, no. 5, pp. 355–365, 2011.
 - [3] E. Mahmoud, E. Masad, and S. Nazarian, “Discrete element analysis of the influences of aggregate properties and internal structure on fracture in asphalt mixtures,” *Journal of Materials in Civil Engineering*, vol. 22, no. 1, pp. 10–20, 2010.
 - [4] Z. You and W. G. Buttlar, “Discrete element modeling to predict the modulus of asphalt concrete mixtures,” *Journal of Materials in Civil Engineering*, vol. 16, no. 2, pp. 140–146, 2004.
 - [5] W. G. Buttlar and Z. You, “Discrete element modeling of asphalt concrete: microfabric approach,” *Transportation Research Record: Journal of the Transportation Research Board*, vol. 1757, no. 1, pp. 111–118, 2018.
 - [6] L. B. Wang, L. A. Myers, L. N. Mohammad, L. N. Mohammad, and Y. R. Fu, “Micromechanics study on top-down cracking,” *Transportation Research Record: Journal of the Transportation Research Board*, vol. 1853, no. 1, pp. 121–133, 2018.
 - [7] V. P. Puzinauskas, “Influence of mineral aggregate structure on properties of asphalt paving mixtures,” *Highway Research Record*, vol. 51, pp. 118–126, 1964.
 - [8] M. Lu and G. R. McDowell, “The importance of modelling ballast particle shape in the discrete element method,” *Granular Matter*, vol. 9, no. 1-2, pp. 69–80, 2007.
 - [9] Z. You, Y. Liu, and Q. Dai, “Three-dimensional microstructural-based discrete element viscoelastic modeling of creep compliance tests for asphalt mixtures,” *Journal of Materials in Civil Engineering*, vol. 23, no. 1, pp. 79–87, 2011.
 - [10] K. Georgouli, A. Loizos, and C. Plati, “Calibration of dynamic modulus predictive model,” *Construction and Building Materials*, vol. 102, pp. 65–75, 2016.
 - [11] X. Li and M. Marasteanu, “The fracture process zone in asphalt mixture at low temperature,” *Engineering Fracture Mechanics*, vol. 77, no. 7, pp. 1175–1190, 2010.
 - [12] D. R. Petersen, R. E. Link, M. P. Wagoner, W. G. Buttlar, and G. H. Paulino, “Development of a single-edge notched beam test for asphalt concrete mixtures,” *Journal of Testing and Evaluation*, vol. 33, no. 6, article 12579, 2005.
 - [13] H. Kim, M. P. Wagoner, and W. G. Buttlar, “Simulation of fracture behavior in asphalt concrete using a heterogeneous cohesive zone discrete element model,” *Journal of Materials in Civil Engineering*, vol. 20, no. 8, pp. 552–563, 2008.
 - [14] H. Kim and W. G. Buttlar, “Discrete fracture modeling of asphalt concrete,” *International Journal of Solids and Structures*, vol. 46, no. 13, pp. 2593–2604, 2009.
 - [15] F. Eckwright, S. J. Jung, and A. M. A. Abdo, “Utilizing a particle flow code in 2dimensional discrete element method of fracture resistance evaluation of HMA and brittle rock,” *Asian Journal of Civil Engineering*, vol. 15, pp. 9–21, 2014.
 - [16] A. K. H. Kwan and C. F. Mora, “Effects of various shape parameters on packing of aggregate particles,” *Magazine of Concrete Research*, vol. 53, no. 2, pp. 91–100, 2001.
 - [17] C. G. Rocco and M. Elices, “Effect of aggregate shape on the mechanical properties of a simple concrete,” *Engineering Fracture Mechanics*, vol. 76, no. 2, pp. 286–298, 2009.
 - [18] S. Adhikari and Z. You, “3D microstructural models for asphalt mixtures using X-ray computed tomography images,” *International Journal of Pavement Research and Technology*, vol. 1, pp. 94–99, 2008.
 - [19] Z. You, S. Adhikari, and Q. Dai, “Three-dimensional discrete element models for asphalt mixtures,” *Journal of Engineering Mechanics*, vol. 134, no. 12, pp. 1053–1063, 2008.
 - [20] Y. Liu, Q. Dai, and Z. You, “Viscoelastic model for discrete element simulation of asphalt mixtures,” *Journal of Engineering Mechanics*, vol. 135, no. 4, pp. 324–333, 2009.
 - [21] D. Y. Wang, W. L. Wu, X. N. Zhang, J. M. Yu, and Z. Li, “Numerical simulation of splitting test of asphalt mixture based on DIP-FEM,” *Journal of Jilin University (Engineering and Technology Edition)*, vol. 41, pp. 968–973, 2011.
 - [22] Y. Y. Li, D. Hu, B. S. Hu, and X. B. Zheng, “The multi-scale numerical analysis of asphalt pavement,” *Northern Communications*, vol. 20, pp. 59–64, 2015.
 - [23] S. G. Hou, K. Xu, and H. Zhang, “Micro-mechanical analysis of uniaxial compression test of asphalt mixtures by discrete element modeling,” *Journal of Nanjing Tech University (Natural Science Edition)*, vol. 37, pp. 73–78, 2015.
 - [24] J. Chen and X. M. Huang, “Simulation of fracture process of asphalt mixture using three-dimension discrete element method,” *Journal of South China University of Technology (Natural Science Edition)*, vol. 40, pp. 21–26, 2012.
 - [25] P. P. Yang, P. Xiao, Y. Ding, and J. H. Zheng, “Microstructure characteristics analysis of asphalt mixture based on the discrete element method,” *Journal of China University of Mining and Technology*, vol. 47, pp. 900–906, 2018.
 - [26] H. Gao, X. H. Yang, and P. Tang, “Discrete element numerical simulation on rutting deformation of asphalt mixture,” *Chinese Journal of Solid Mechanics*, vol. 40, pp. 21–26, 2012.
 - [27] B. Zhou, H. B. Wang, W. F. Zhao, J. W. Li, and B. C. Zheng, “Analysis of relationship between particle mesoscopic and macroscopic mechanical parameters of cohesive materials,” *Rock and Soil Mechanics*, vol. 33, pp. 3171–3175, 2012.
 - [28] F. Z. Shi, M. F. Chang, J. Z. Pei, Y. P. Sheng, and Q. Z. Dong, “Mesoscopic analysis on vector field of asphalt mixture using discrete element method,” *Journal of Chang’an University (Natural Science Edition)*, vol. 34, pp. 9–15, 2014.
 - [29] F. Li, C. W. Shen, and J. X. Yang, “Research on numerical simulation of micro-mechanics damage of asphalt concrete,” *Transportation Science & Technology*, vol. 1, pp. 56–58, 2006.
 - [30] L. W. Shi, D. Y. Wang, C. Xu, and H. H. Liang, “Investigation into meso performance of asphalt mixture skeleton based on discrete element method,” *Journal of South China University of Technology (Natural Science Edition)*, vol. 43, pp. 50–56, 2015.
 - [31] X. H. Ma and L. H. Li, “Analysis of void characteristics of asphalt mixtures with discrete element method mode,” *Journal of Tong-ji University (Natural Science)*, vol. 41, pp. 1830–1836, 2013.
 - [32] S. G. Hou, “Viscoelastic analysis of asphalt mixture based on dynamic creep test,” *Journal of Nanjing University of Technology (Natural Science Edition)*, vol. 32, pp. 33–36, 2010.
 - [33] J. Chen and X. M. Huang, “Virtual fatigue test of asphalt mixture based on discrete element method,” *Journal of Jilin University (Engineering and Technology Edition)*, vol. 40, pp. 435–440, 2010.
 - [34] Y. Z. Chen and Z. X. Li, “Meso-structure of crumb rubber asphalt mixture based on discrete element method,” *Journal of Harbin Institute of Technology*, vol. 45, pp. 116–121, 2013.
 - [35] J. Zhou, Q. Tian, Y. Q. Rui, and H. Ying, “A dem geometric modeling method of HMA based on digital imaging

- processing,” *Journal of Civil Architectural & Environmental Engineering*, vol. 34, pp. 136–140, 2012.
- [36] D. Y. Zhang, X. M. Huang, and Y. Gao, “Three dimension virtual uniaxial creep test of asphalt mixture by using discrete element method,” *Journal of South China University of Technology (Natural Science Edition)*, vol. 40, p. 15, 2012.
- [37] Li. Tian, Yu. Liu, and B. G. Wang, “3D DEM model and digital restructure technique for asphalt mixture simulation,” *Journal of Chang’an University: Natural Science Edition*, vol. 27, pp. 23–27, 2007.
- [38] J. Yang, Xu. Zhang, and H. R. Zhu, “Discrete element simulation on tri-axial shear test of asphalt mixtures,” *Journal of Building Materials*, vol. 15, p. 64, 2012.
- [39] X. G. Hu, “Review on asphalt mixture micromechanics analysis,” *Journal of Chang’an University: Natural Science Edition*, vol. 25, pp. 6–9, 2005.

